

Determination of Thermal Accommodation Coefficients on CaSiO_3 and SiO_2 using Molecular Dynamics and Experiments

D. Bayer-Buhr^{a,*}, M. Vimal^b, A. Prakash^{b,*}, U. Gross^a, T. Fieback^a

^a*Technische Universität Bergakademie Freiberg, Chair of Technical Thermodynamics,
Gustav-Zeuner-Str. 7, 09599 Freiberg, Germany*

^b*Technische Universität Bergakademie Freiberg, Micromechanical Materials Modelling (MiMM),
Lampadiusstr. 4, 09599 Freiberg, Germany*

Abstract

The thermal accommodation coefficient α has been assumed, although lacking any experimental proof, to be near unity for most gases so far, which denotes no influence. However, it plays a contributing role in the field of the effective thermal conductivity of highly porous insulation materials based on SiO_2 or CaSiO_3 as it is shown in this work. Besides, this work investigates a possible influence on α for Ar , N_2 , He within parameters like temperature, roughness and contamination as this has not been examined on such materials so far. More importantly, it answers the question whether the assumption of $\alpha = 1$ is valid.

By using a parallel plates device, very similar to the guarded-hot-plate, following EN 12667 it was possible to determine α on a dense CaSiO_3 . It occurred that the assumptions $\alpha = 1$ (for Ar , N_2) and $\alpha = 0.3$ (for He) are valid for measurements near room temperature. Further, physical adsorption was found to increase α . The determination of the influence of roughness has been started showing an interesting effect, but it still remains an open topic.

In a collaborative study molecular dynamics (MD) simulations were performed showing a strong equivalence of α between SiO_2 and CaSiO_3 . These results can be considered a lower limit of α as neither roughness nor adsorption processes have been included in the simulation. Therefore, any deviations between experiments and MD could be considered as an appearance of physical adsorption.

Keywords: insulation materials, thermal accommodation coefficient, thermal conductivity, molecular dynamics

*Corresponding author

Email addresses: bayerd@mailserver.tu-freiberg.de (D. Bayer-Buhr), Arun.Prakash@imfd.tu-freiberg.de (A. Prakash)

URL: <https://tu-freiberg.de/fakult4/iwtt/ttd> (D. Bayer-Buhr)

1. Introduction

Facing today's need for increased energy efficiencies of industrial processes, the thermophysical properties of insulating materials have evoked great interest for decades. Especially new kinds of insulation materials like aerogels or highly porous calcium silicates ($CaSiO_3$) show promise in reducing heat transfer due to their high porosity and pore sizes in the micro and meso range [1]. Unfortunately, there is still a lack of understanding of heat transfer due to the very heterogeneous structure of such materials. Some efforts were made by Swimm [2] who developed a model for the description of heat transfer in such materials. Following Swimm [2] it can be shown that with the usual parallel and series connection of the various heat transfer mechanisms (solid and gas conduction, radiation) the effective thermal conductivity was expected to be lower than the experimental results indicated. With introduction of a coupling factor dependent on the material, their model reflects real-world experimental results.

One detail of the model of Swimm [1] or others (e.g. Zhao [3]), which remains unverified until now and may be questioning the models of the effective thermal conductivity, is the influence of the thermal accommodation coefficient α within the gas conduction, which is assumed to be unity for porous insulation materials so far [1, 3, 4]. In literature, merely few results are available for silicium oxide (SiO_2 , amorphous [5], quartz [6]) and none for calcium silicate providing only a weak basis for the models of the effective thermal conductivity. Therefore, the goal of this work is to shed light on the situation of the thermal accommodation coefficient on amorphous SiO_2 and $CaSiO_3$ as they usually are the main components in conventional and highly porous insulation materials. More importantly, it provides the necessary basis of whether $\alpha = 1$ is valid. Furthermore, the influence of temperature, roughness and contamination is examined.

As the experimental determination of the thermal accommodation coefficient is always influenced by contributing factors (e.g. surface roughness, adsorption layers), which leads usually to an increase of the thermal accommodation coefficient, a collaborative study using molecular dynamics (MD) was done for comparison to get a more detailed look onto the situation at an atomistic level. This gives a first hint, in what range of values α could be expected, as the results of MD can be considered as the lower limit of the thermal accommodation coefficient on amorphous SiO_2 and $CaSiO_3$. Using MD, many studies have been conducted previously to determine the accommodation coefficient values for different solid-gas molecule combinations (e.g. amorphous silica aerogels [7] or amorphous polystyrene [8], crystal [9]). However, the study of Zichunyang et al [7] neglects the influence of the attractive forces of the solid atoms between neighboring nanoparticle interfaces. As explained above, Swimm [2] was able to clearly show that a coupling factor has to be introduced in order to represent this improved heat transfer. Due to the neighboring nanoparticle interfaces the attractive forces tend to overlap and increase, which leads to a higher adsorption potential and thus to a higher value of α . Apart from predicting the values of α , the influence of surface roughness [10], gas-wall interaction strength [11, 12, 9], gas molecular mass [12, 13] and gas temperature [13] on α have also been studied using MD. Higher solid wall surface roughness increases the number of gas-wall collisions through interaction of

gas molecules with the lateral edges of the solid atoms [9], thus increasing α values. Therefore, MD has shown to be a very good, although also very time-consuming tool, for completing the picture of thermal accommodation coefficients on solid surfaces in comparison to experimental observations.

The paper is structured as follows: First, an overall description of the examined insulation materials is given as well as a short summary of the setup of the experimental device. After this a brief description of the MD is given. The final comparison and discussion with experimental and MD results will be presented at last.

2. Characterization of Porous Media

The materials which were examined are conventional highly porous insulation materials for high temperature usage purposes as well as sintered samples composed of SiO_2 and $CaSiO_3$ (see Table 1 for composition). The pore size, that shows major effects on the pressure dependent effective thermal conductivity λ_{eff} [1], ranges from macropores for the porous calcium silicates with a sharp pore size distribution to macro- and mesopores for the porous silicium oxides with a broad pore size distribution. During the experiments the Knudsen effect, where λ_{eff} begins to develop a pressure-dependency [14], appeared by lowering the pressure. Measurements of the surface roughness (R_z) revealed no clear correlation between porosity and roughness, although all highly porous samples were treated the same way (trimming). Sample $CaSiO_3$ D1 was polished with a diamond abrasive paper, but didn't show any significant difference in roughness in comparison to the other samples.

All samples are 100 mm in diameter with a height of 5-7 mm. Four thermocouples boreholes (\varnothing 1.1 mm) were drilled horizontally to minimize heat losses by leading the thermocouples along isotherms.

Table 1: Pore sizes, porosities (measured with mercury intrusion porosimetry), composition and surface roughness (R_z , measured with tactile incision technique) of used materials

material	pore size [nm]	porosity [%]	surface roughness [μ m]	composition
$CaSiO_3$ A	320 & 700	88	17.705	80% $CaSiO_3$, 10% Zr, 10% Residuals
$CaSiO_3$ B	530 & 1360	88	26.423	91% $CaSiO_3$, 9% Residuals
$CaSiO_3$ C	350	86	39.706	100% $CaSiO_3$
$CaSiO_3$ D1	n.a.	less than 5	36.120	100% Wollastonite
$CaSiO_3$ D2	n.a.	less than 5	n.a.	100% Wollastonite
SiO_2 A	22 & ca. 2000	81	24.875	80% SiO_2 , 15% $ZrSiO_4$, 5% Residuals
SiO_2 B	15 & ca. 780	86	19.865	80% SiO_2 , 20% SiC

Concerning the preparation of the sintered sample ($CaSiO_3$ D1, wollastonite) the following procedure has

been performed: 250 g wollastonite¹ Casiflux (Sibelco) and 2.5 g TiO₂ R 320 (Sachtleben) (used as a sintering aid) were mixed with 100 g deionized water for at least 1 hour. In order to obtain a castable slurry, additives were added to the slurry: 2.5 g Optapix AC 170 (Zschimmer & Schwarz, Germany), 0.5 g Axilat RH 50 MD (C.H. Erbslöh, Germany), and 1 g Castament F60 (BASF Construction Solutions GmbH, Trostber, Germany). The Optapix AC 170 was used as a binder, the Castament F60 acted as dispersant and the Axilat were added to change the dilatant behavior of the slurry to obtain a shear thinning behavior which is necessary for the casting process. The slurry was cast into the casting mold, which is basically of the same form as the porous samples (ø 100 mm, height 7 mm). The sample was dried carefully at 50°C and sintered at 1200°C for 3 hours. The porosity is assumed to be significantly lower (less 5%) than for the other porous samples.

3. Experimental Setup and Mathematical Foundation

For the determination of thermal accommodation coefficients on amorphous SiO_2 and $CaSiO_3$ a measurement device similar to the well-known steady-state guarded-hot-plate device [15] with parallel plates was developed and built. It will be presented in the following. After this a more detailed description of the test procedure and the extraction of the thermal accommodation coefficient from experimental measurements are given.

3.1. Setup

A schematic of the experimental setup is shown in Figure 1. The underlying idea of this method is the use of guarding heat foils (HK2/3/6) based on superthin polyimide foil (less than 0.2 mm thick) surrounding the measuring heat foil (HK1) in the center. Thus, an isothermal zone is created to ensure that the heat flow which is needed for the derivation of the thermal accommodation coefficient is one-dimensional through the gas gap (2 mm). The temperature difference over the gas gap is 10 K controlled by the underlying heat foil (HK4). The gas gap is confined above by a reference sample which is held in place by the upper plate assembly and below by the ceramic sample which is placed above HK4. Therefore, the thermal accommodation coefficient of the ceramic material α_c is determined in dependence of the thermal accommodation coefficient of the reference sample α_r . The latter is determined during calibration. For thermal separation the upper plate assembly is held in position by a linear translator which is placed above the vacuum chamber. The vacuum chamber is cylindrical with a height of 300 mm and a diameter of 200 mm. It can be opened vertically and it holds a pressure of 10^{-4} mbar. The essential water-cooled heat sink is placed below heat foil HK4 and provides the lowest temperature in the system (for more details see [16]).

¹Wollastonite is the natural form of $CaSiO_3$.

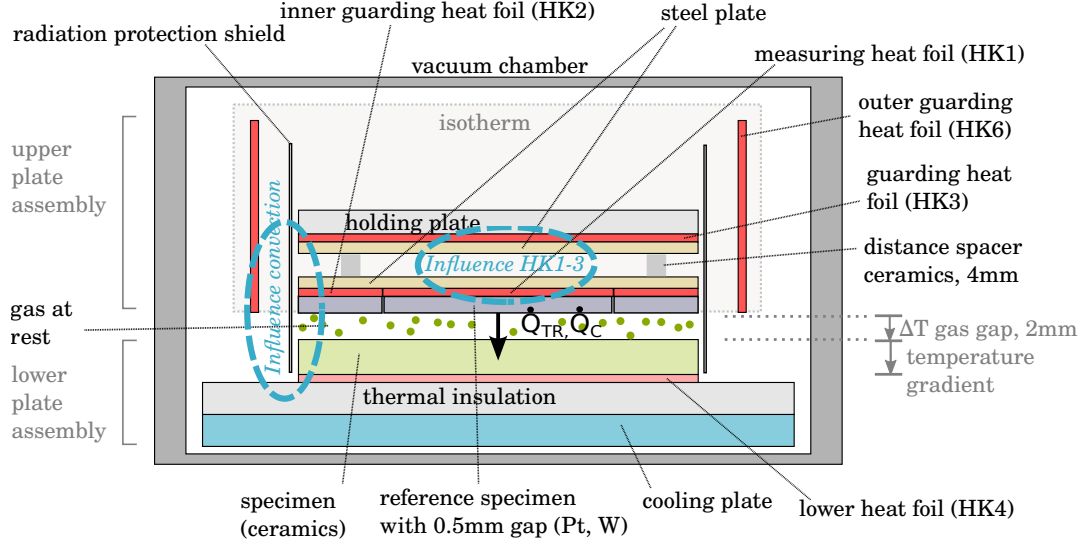


Figure 1: Scheme of the developed measurement device, similar to guarded-hot-plate regarding [15]; \dot{Q}_{TR} is the heat flow in the transition regime, \dot{Q}_C is the heat flow in the continuum regime; each measurement is performed at least twice to ensure repeatability; the temperature level is $t_{upper}/t_{lower} = 75/65^\circ\text{C}$

3.2. Test Procedure and Determination of α

The measurements start with baking-out at 140°C and evacuation down to the lowest possible pressure (ca. 10^{-4} mbar) for at least 12 h. Further the atmosphere is flushed and evacuated twice more very rapidly to make sure that gas residuals are flushed out of the vacuum chamber. After this atmospheric cleaning process, four steady-state conditions at different pressures are generally reached at a constant temperature of at least 60 minutes, each between 3 - 30 mbar for Ar and N_2 as well as 5 - 300 mbar for He . During the measurement all signals like current and voltage for calculation of the power of HK1 as the heat flow rate applied for the thermal accommodation coefficient determination, temperature readings of about 30 thermocouples, and inside pressures are logged every 10 s. The measured pressure value is needed to control the stability of the gas regime and for the calculation of the Kn -number. Additionally the thermocouples provide an overall picture of the thermal homogeneity to ensure the validity of the underlying parallel plate principle. In order to separate the radiation component from the measured heat flow, the radiation is estimated and subtracted from the measured heat flow. A measurement at very low pressures without any influences of gas thermal conduction was not possible, as will be explained below. (Rev 2, pt 4)

Two phenomena which were observed during calibration led to a confined measurability and will be presented more in detail in the following as this helps to get an impression on the challenging aspects of this project:

Mutual influences between HK1 and HK3. The task of HK3 is to provide a $\Delta T = 0\text{ K}$ (temperature difference) next to HK1 as the measuring heat foil. Unfortunately, it turned out that the thermal resistivity of the layer

in between HK1-3 had to exhibit a very high level to fulfill this task. After testing different materials the best option was to create a larger gas gap of 4 mm (see Figure 1) by using ceramic distance spacers. The idea for this can be followed in Figure 2, where the well-known S-curve of the pressure dependent gas thermal conductivity can be seen versus logarithmic pressure: The gas thermal conductivity in the 2 mm gap varies during the measurement depending on the pressure (blue curve) whereas in the 4 mm gap (green curve) there is an almost pressure-independent gas thermal conductivity. Thus, only the 2 mm gap gas conduction shows a pressure-dependent behaviour which is needed to derive the thermal accommodation coefficient. Below the lower pressure limit an influence of the pressure-dependent thermal conductivity within the 4 mm gap starts to develop, which leads to an incorrect measurement of the heat flow of HK1, which is needed for the derivation of α . This phenomenon therefore defines a lower pressure limit for the measurability of the device.

Influence of convection. Another phenomenon defines the upper limit of measurability of the device. The radiation protection shield consists of a very thin metal foil, which is very flexible. Therefore, due to all the wiring of thermocouples, it is not possible to place the shield in an exact position. By means of numerical investigations it can be shown that near atmospheric pressure natural convection develops in the annulus. Since the gap between the radiation protection shield and the thermal insulation below HK4 is not completely closed, an accelerated flow occurs at the outer edge of HK2, which leads to increased heat losses. Since HK2 has to compensate for this heat loss in order to maintain $\Delta T = 0$ K, the power of HK2 increases. At the same time, the power of HK1 decreases because it is not exposed to the same heat loss as HK2. Due to this, the power of HK1 decreases at higher pressures, as can be seen in Figure 2. As the lower and upper limit are also dependent on the kind of gas, different upper pressure limits could be found ranging from 3 mbar for *Ar* up to 300 mbar for *He*.

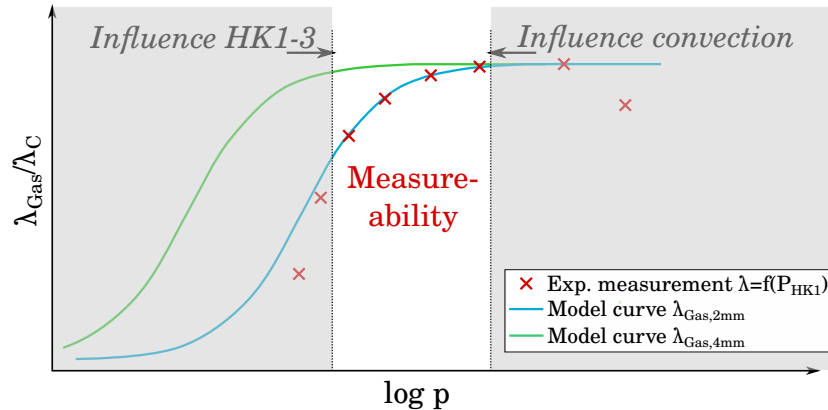


Figure 2: Schematic measurability of the measuring device; two occurring phenomenon leading to upper and lower limit of measurability; y-axis: λ_{Gas} is the gas thermal conductivity at arbitrary pressure, λ_C is the gas thermal conductivity in continuum range, x-axis: logarithmic pressure p ; P_{HK1} = power of HK1

For calculation of the thermal accommodation coefficient the model of Springer [17] is followed, which extends the closed-form solution of heat conduction in rarefied gases between parallel plates developed by Lees and Liu [18] to arbitrary values of the thermal accommodation coefficient:

$$\frac{\dot{Q}_{TR}}{\dot{Q}_{FM}} = \left(1 + \frac{4}{15} \frac{1}{Kn} \frac{\alpha_r \alpha_{cer}}{\alpha_r + \alpha_{cer} - \alpha_r \alpha_{cer}}\right)^{-1} \quad (1)$$

with \dot{Q}_{TR} and \dot{Q}_{FM} as the heat flow rates by conduction through the gas in the transition regime and in the free molecular regime. Respectively, Kn is the Knudsen number and α_r and α_{cer} is the thermal accommodation coefficients on the upper/reference and lower/ceramic plate. With the help of Sherman's interpolation [19],

$$\frac{\dot{Q}_{TR}}{\dot{Q}_{FM}} = \left(1 + \frac{\dot{Q}_{FM}}{\dot{Q}_C}\right)^{-1} \quad (2)$$

where \dot{Q}_C is the heat flow rate by conduction through the gas in the continuum regime, one can obtain the following equation for experimental determination of the thermal accommodation coefficient (at constant temperature difference):

$$\frac{\dot{Q}_{TR}}{\dot{Q}_C} = \left(1 + \frac{15}{4} Kn \frac{\alpha_r + \alpha_{cer} - \alpha_r \alpha_{cer}}{\alpha_r \alpha_{cer}}\right)^{-1} \quad (3)$$

As α is always influenced by the temperatures of the gas and wall molecules as well as by the composition, the surface structure and eventual contamination of the wall material, two different accommodation coefficients are present in a parallel plates setup. If the surfaces confining the gas gap are similar (same material and surface treatment) one can assume: $\alpha_{r,1} = \alpha_{r,2} = \alpha_r$. This gives a simpler version of Equation 3:

$$\frac{\dot{Q}_{TR}}{\dot{Q}_C} = \left(1 + \frac{15}{4} Kn \frac{\alpha_{r,1} + \alpha_{r,2} - \alpha_{r,1} \alpha_{r,2}}{\alpha_{r,1} \alpha_{r,2}}\right)^{-1} = \left(1 + \frac{15}{4} Kn \frac{2 - \alpha_r}{\alpha_r}\right)^{-1} \quad (4)$$

As observed during measurements the temperature difference across the gas gap changes due to a pressure-dependent contact resistance between the heat foil and the sample for the lower plate. Therefore, this influence has to be corrected leading to the following equation, which is used for calibration:

$$\boxed{\frac{\dot{Q}_{TR}}{\dot{Q}_C} * \frac{\Delta T_C}{\Delta T_{TR}} = \left(1 + \frac{15}{4} Kn \frac{\alpha_{r,1} + \alpha_{r,2} - \alpha_{r,1} \alpha_{r,2}}{\alpha_{r,1} \alpha_{r,2}}\right)^{-1} = \left(1 + \frac{15}{4} Kn \frac{2 - \alpha_r}{\alpha_r}\right)^{-1}} \quad (5)$$

where ΔT_C and ΔT_{TR} represent the temperature differences over the gas gap in the continuum and transition regime, respectively. By measuring the ceramic sample the equivalent equation is used:

$$\boxed{\frac{\dot{Q}_{TR}}{\dot{Q}_C} * \frac{\Delta T_C}{\Delta T_{TR}} = \left(1 + \frac{15}{4} Kn \frac{\alpha_r + \alpha_{cer} - \alpha_r \alpha_{cer}}{\alpha_r \alpha_{cer}}\right)^{-1}} \quad (6)$$

By choosing a certain thickness of the gas gap (here: 2 mm) and different pressure values the transition and continuum gas state can sequentially be reached in the vacuum chamber. For finally calculating α_r or α_{cer} they are determined equivalently based on Equation 5 or 6, respectively, where α_r or α_{cer} is fitted onto the experimental results with the help of the nonlinear Levenberg-Marquardt regression method [20].

4. Molecular Dynamics Study

A setup similar to the experimental one is created and presented below together with a description of the method used to calculate α_{cer} . Finally, used potentials and parameters, that have been validated with literature are shown. To validate the used calculation method of α_{cer} on amorphous SiO_2 and $CaSiO_3$ the method was tested with tungsten ($W - Ar$ and $W - He$), since reliable literature data are available for these.

4.1. Setup

For generating the amorphous structures of SiO_2 and $CaSiO_3$, the melt-quench process is followed. The starting structure is created by randomly distributing 37,500 ($CaSiO_3 \rightarrow 7,500 - Ca; 7,500 - Si; 22,500 - O$) or 38,400 ($SiO_2 \rightarrow 12,800 - Si; 25,600 - O$) ions in a box of $\approx 10 \times 10 \times 5$ nm based on the reference densities [21, 22] with periodic boundary conditions. The time-temperature cycle for the entire melt quench process considered by Mead [21] ($CaSiO_3$) or Munetoh [22] (SiO_2) is followed. Tungsten, with a body centered cubic structure and same sample dimensions as in the amorphous structure case, is constructed by orienting the densely packed plane (110) along the z direction of the simulation box. The structures are well equilibrated at 300 K and at zero pressure in a NPT ensemble for 160 ps. These final equilibrated structures of amorphous SiO_2 , $CaSiO_3$ and W are used as the solid substrates for their respective simulations (see Figure 3).

The distance between the upper (hot) and lower (cold) plate is maintained at 100 Å for simulations involving Ar & N_2 gas molecules and 1000 Å for He gas molecules to maintain the total gas pressure below their corresponding critical pressures. The solid plates are placed in such a way that the gas interacting surfaces have identical amorphous surfaces at the top and bottom, i.e. the upper plate is just the mirror copy of the lower plate about the center of simulation box. Periodic boundary conditions are applied along x, y and z directions to facilitate the use of PPPM long range solvers. The atoms present within 3.0 Å distance from the outermost layer of walls are fixed to prevent the walls from sliding along the z direction due to gas pressures. Along the z direction for a distance of 20 Å beyond the fixed layers of atoms, vacuum is maintained to prevent energy exchange between the hot and cold plates across the periodic boundary.

In an equilibrium MD for computing α_{cer} , the temperatures of the hot and cold plates need to be maintained at a preset temperature throughout the complete production run. Thermostetting the entire solid plates using a deterministic Nosé-Hoover (NH) thermostat [23, 24], which can preserve the structural properties, could be a viable option. But since the energy/momentum exchange between the solid & gas molecules is the predominant process in this simulation, the NH thermostat preserves the dynamical properties only under certain circumstances. It is indeed a recommended practice to turn off the thermostats before the production run for applications where the dynamical properties are sampled [25]. So, in order to maintain the temperature and to have the gas-wall interaction region to be more physical by preserving both the structural as well as the dynamical properties during the production run, the solid plates are split equally

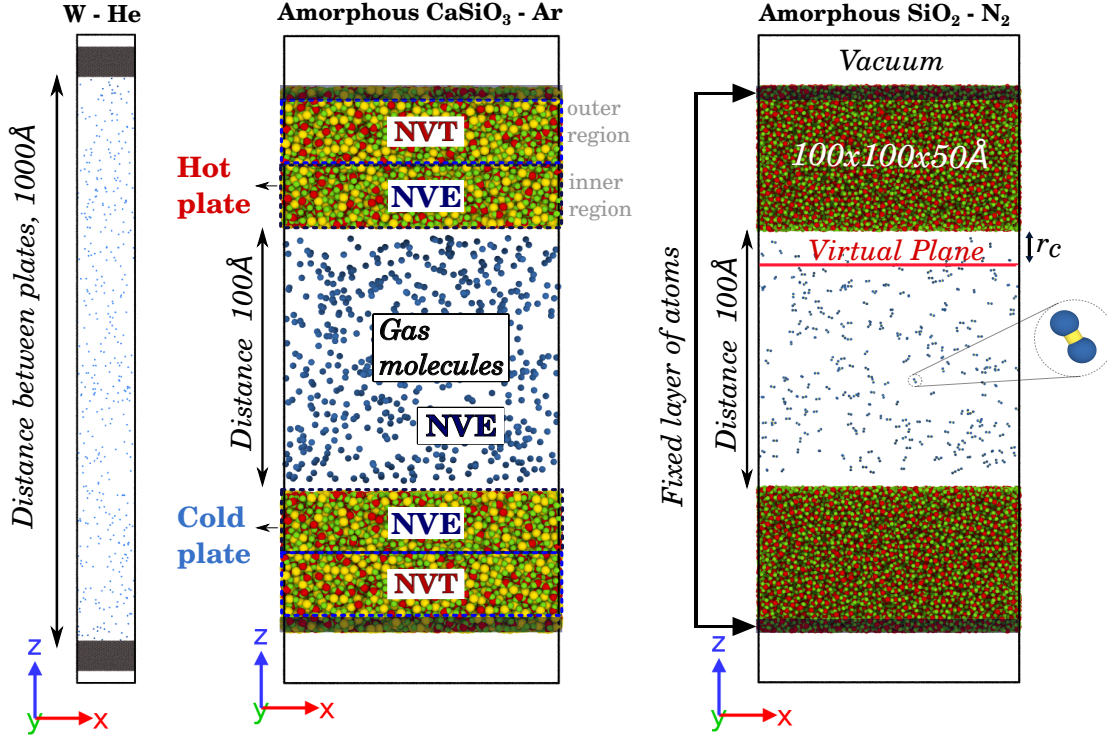


Figure 3: Representative overview of MD cases for amorphous SiO_2 , CaSiO_3 and crystalline W ; parallel plates setup; NVE/NVT for all cases; position of virtual plane at one cutoff-distance r_c for all cases; simulation for all He -cases with wider distance to ensure similar Kn -numbers in comparison to Ar/N_2 -cases (for He - 1000 Å, for Ar and N_2 - 100 Å); Other cases ($\text{CaSiO}_3\text{-He}$, $\text{CaSiO}_3\text{-N}_2$, $\text{SiO}_2\text{-Ar}$, $\text{SiO}_2\text{-He}$, W-Ar) follows identical simulation setups as in the representative cases; Color code for atoms: red-silicon, green-oxygen, yellow-calcium, black-tungsten.

into two regions along the z direction where one region is maintained under micro-canonical (NVE) ensemble that contains the gas-wall interaction surface and the other maintained under the canonical (NVT) ensemble conditions where the temperatures are controlled using Nosé-Hoover thermostat throughout the entire simulation time. An initial equilibration time of 500 ps is allowed for the heat to transfer from the outer to inner region, such that both the NVT & NVE regions attain the same temperature.

The outer regions of the hot and cold plates are maintained at 350 K and 340 K, respectively, to reflect experimental conditions. Further, the influence of temperature levels close by (± 20 K) did not reveal a great effect on α_{cer} and so this parameter variation is neglected in the following (see Figure 4).

After the equilibration of solid plates, the gas molecules are introduced in-between the plates at random positions. An appropriate gas molecule density has to be chosen due to the trade-off involved between increasing the number of gas-wall collisions within the finite simulation time and maintaining the gas pressure below the critical pressure. The number of gas molecules to be introduced is determined by considering the critical pressure of the gases ($p_{\text{cr}} = 4.86$ MPa for Ar , $p_{\text{cr}} = 0.23$ MPa for He , $p_{\text{cr}} = 3.4$ MPa for N_2) as the upper limit and also by taking the Knudsen number ($\text{Kn} = 0.3$ for Ar and N_2 and $\text{Kn} = 0.65$ for He) in the transition flow regime into account.

During both the solid and gas molecules initialization, in order to obtain the Maxwell-Boltzmann distribution for the velocities, random values are sampled from a Gaussian distribution for each velocity component with a mean of 0.0 and a standard deviation scaled to their respective temperatures.

The gas molecules are maintained under NVE ensemble conditions and 1 ns of simulation time is allowed to equilibrate the gas temperature. The extraction of the trajectories of gas atoms for computing α_{cer} starts only after the 1.5 ns of the total equilibration time.

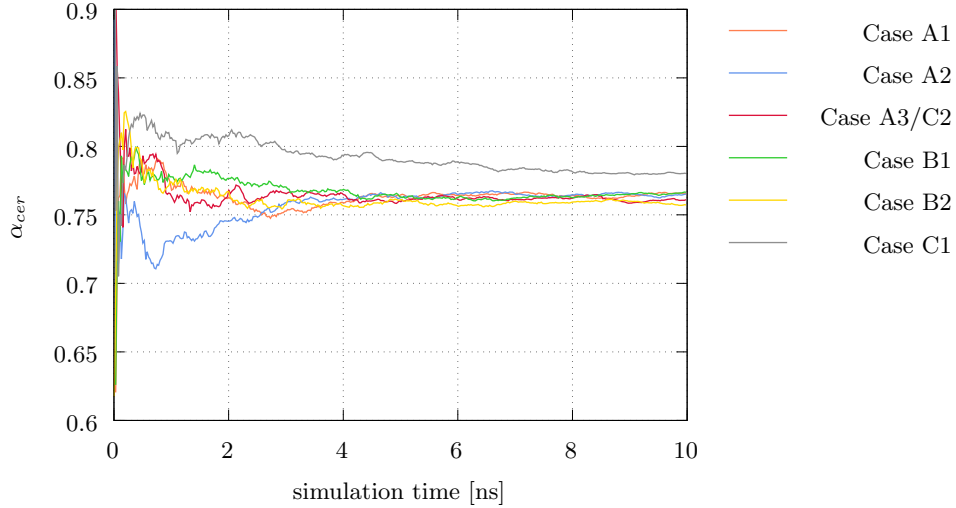


Figure 4: Influence of thermostats, initial seed velocity distribution and temperature level on α_{cer} ; Case A1: Berendsen thermostat, $\alpha_{cer} = 0.765$; Case A2: Langevin thermostat - $\alpha_{cer} = 0.766$; Case A3/C2: Nosé-Hoover thermostat/temperature level 340/350 K - $\alpha_{cer} = 0.761$; Case B1: initial seed velocity distribution 1 - $\alpha_{cer} = 0.766$; Case B2: initial seed velocity distribution 2 - $\alpha_{cer} = 0.757$; Case C1: temperature level 310/320 K - $\alpha_{cer} = 0.78$

4.2. Calculation of α_{cer}

For computing of α_{cer} , a virtual plane (see Figure 3) is constructed at a distance of one gas-wall interaction cut off radius (r_c) away from the inner surface of the upper solid wall normal to the z direction, to avoid any influence of the attractive forces from the solid wall atoms [10, 11, 13]. Gas atoms crossing the virtual plane towards the solid wall with positive z velocities ($v_z > 0$) are categorized as incident atoms, which represents the start of the energy exchange process. The same gas atoms recrossing the virtual plane after having collided with the solid wall with negative z velocities ($v_z < 0$) are categorized as reflected atoms, which represents the end of the energy exchange process. This is based on the assumption that the probability of gas-gas collisions within the upper solid wall and the virtual plane region is negligible, i.e. gas atoms crossing the virtual plane will return back only after having direct collision with the solid wall atoms [13]. Only the velocities of gas molecules crossing this virtual plane at any time step are considered for calculating α_{cer} . For the case of monoatomic molecules such as Ar and He , the positional coordinates and velocities of atoms crossing the virtual plane are directly exported whereas for the case of diatomic molecules such as N_2 , the

positional coordinates and velocities at the geometric center of mass (COM) of the diatomic molecules [7] are exported and only based on the COM, a molecule is checked whether it has crossed the virtual plane or not during the simulation. The formula for calculating α_{cer} from Spijker [26], based on the least squares approximation on the collision data containing incident (K_I) and reflected (K_R) quantities is given by,

$$\alpha_{cer} = 1 - \frac{\sum_i (K_I^i - \langle K_I \rangle) (K_R^i - \langle K_R \rangle)}{\sum_i (K_I^i - \langle K_I \rangle)^2} \quad (7)$$

where the summation is performed over all the recorded collisions for the considered quantity (kinetic energy). To allow a sufficient number of gas-wall collisions so as to achieve good statistics for the α_{cer} calculations, the total simulation time is chosen based on the convergence of the α_{cer} value with respect to simulation time. All the simulations are performed with a time step of 1 fs (except 0.5 fs for the amorphous SiO_2 system) using the LAMMPS package [27] and post processing & visualization have been done using the open source visualization tool OVITO [28].

4.3. Interatomic Potentials and Parameters

The interatomic potentials used for the amorphous SiO_2 , $CaSiO_3$ and W as well as for the gases Ar , He and N_2 are listed in Table 2. The potential expression of $CaSiO_3$ [29] involves a dispersion term in addition to a long-range Coulombic term and a short-range Morse function. The addition of the repulsive term is necessary to model interactions at high temperatures and pressures. Simulating using potentials without the repulsive contribution term for cases where the ions tend to come close enough, i.e. at elevated temperatures and during interactions with fixed layer of atoms, could be problematic due to the unphysical attraction values at low inter-ionic distances. For the evaluation of long range Coulombic interactions, a particle-particle-particle mesh (PPPM) over the standard Ewald summation method is chosen for its computational efficiency with a force norm of less than 10^{-6} eV/Å. To avoid the computation of long range coulombic interactions, a 3-body Tersoff potential for SiO_2 [22] over the Beest-Kramer-Santen (BKS) or Morse potential is used. Lennard-Jones (LJ) [12-6] potential [30] is widely used to model gas-gas and gas-wall interactions. Each N_2 molecule is modeled as a rigid rotor with a fixed bond length of 1.1 Å [13]. The parameter values for gas-wall interactions can be calculated by using the approximation methods like Fender-Halsey (FH) and Lorentz-Berthelot (LB) mixing rules. Since the LB mixing rule is observed to overestimate the gas-wall atoms bonding characteristics [11], parameter values in the current simulations are calculated using the FH mixing rule. Cut-off radius for gas-gas and gas-wall interactions are 2.5 times σ_{ii} [11] and 8 Å, respectively. The LJ parameter values chosen for Ca , Si and O atoms are successfully used to study the physical adsorption behavior of gases on to the amorphous silica, silicate glass surfaces and zeolites [31, 32]. LJ parameter values ($\epsilon_{W-Ar} = 0.002168$ eV & $\sigma_{W-Ar} = 2.93$ Å) used in the tungsten surface scattering studies [33] are employed for $W-Ar$ interactions. For $W-He$, the functional form and parameter values used in tungsten and helium interaction studies [34] are chosen. The cutoff radii for tungsten-argon and tungsten-helium interactions are

6 Å and 4 Å respectively. All potentials and parameter values are substantially tested and validated with their corresponding literature.

5. Results

In the following, the results obtained from MD and experiments for validation with W as well as for amorphous SiO_2 and $CaSiO_3$ are presented.

5.1. Validation with Tungsten - Experiments and Molecular Dynamics

In Figure 5 literature data in comparison with the results from experiments and MD are shown. Basically the data from literature scatters very much, but some trends are visible. For $W - Ar$, the desorption of Ar is evident with a strong decreasing trend with increasing temperature above 87 K, the condensation temperature of Ar [42]. In contrast, it is evident that there is no decreasing trend for $W - He$ due to the non-adsorptive behavior of He . Furthermore, literature data varies between 0 to 1 over the entire temperature range. Usually this behavior is explained with adsorption effects of unknown nature (e.g. Saxena & Joshi [6]). For the validation with W (red triangles for exp., orange triangles for MD) the results from MD agree very well with literature data. Therefore, the method to derive the thermal accommodation coefficient from MD (following Spijker [26]) is validated.

Further, results from the experimental calibration indicate at least chemical adsorption at the W surface leading to a higher α_r . Steinbeck [43] as well as Saxena & Joshi [6] revealed that W creates tungsten oxide as well as tungsten nitride under the exposure of N_2 & O_2 . Less influence of adsorption during the calibration was observed with platinum (Pt) confirming the calibration of the measurement device (not shown).

5.2. Molecular dynamics

Results of MD for amorphous SiO_2 and $CaSiO_3$ are presented in Figure 6. According to the model of Spijker [26] the velocities of the incoming and outgoing atoms passing the virtual plane are tracked and used for the calculation of α_{cer} via a linear least squares approximation. By looking at the resulting plots it might be obvious that for smaller α_{cer} (e.g. $SiO_2/CaSiO_3$ -He) the cluster of most points has a more elliptical shape than for a higher value of α_{cer} where it forms a circle. This is in accordance with Spijker [26]. The limits of α_{cer} being 0 or 1 present themselves as dashed lines whereas the red line represents the final result of the linear least squares approximation. The slope of the red line gives α_{cer} . Note that with an increasing slope α_{cer} decreases. Further, it appears that the results are quite equal for SiO_2 and $CaSiO_3$ for each gas. Only with decreasing atomic weight of the gas the deviations of α_{cer} between SiO_2 and $CaSiO_3$ increase significantly, but very slightly as with $CaSiO_3$ exhibiting the lower α_{cer} . It is found that the effect of the

Table 2: Overview of interatomic potentials and parameters used for MD; all validated with literature

Interatomic potentials				
$CaSiO_3$ [29]	$U(r) = \frac{z_i z_j e_{ecc}^2}{r} + D_{ij} \{ [1 - e^{-a_{ij}(r-r_0)}]^2 - 1 \} + \frac{C_{ij}}{r^{12}}$ where D_{ij} is the bond dissociation energy, a_{ij} is a function of the slope of the potential energy well, C_{ij} is the repulsive contribution parameter, r_0 is the equilibrium bond distance, z is the ionic charge and e_{ecc} is the elementary charge constant.			
Ion pair	D _{ij} [eV]	a _{ij} [Å ⁻¹]	r ₀ [Å]	C _{ij} [eV Å ¹²]
$Si^{+2.4} - O^{-1.2}$	0.340554	2.006700	2.100000	1.0
$Ca^{+1.2} - O^{-1.2}$	0.030211	2.241334	2.923245	5.0
$O^{-1.2} - O^{-1.2}$	0.042395	1.379316	3.618701	22.0
SiO_2 [22]	$E = \frac{1}{2} \sum_i \sum_{j \neq i} V_{ij}$ where E is the potential energy (more details in [35]). Parameter set developed by Munetoh [22] is used.			
W [36]	$E = \sum_i G_i \left(\sum_{j \neq i} \rho_j^a(r_{ij}) \right) + \frac{1}{2} \sum_{i,j (j \neq i)} U_{ij}(r_{ij})$ where r_{ij} is the distance between atoms i & j , G is the embedding energy, ρ^a is the spherically averaged atomic electron density and U_{ij} is the pair-wise potential interaction between atoms i & j . For defining the interaction between tungsten atoms, the EAM potential parameters developed by Olsson [37] have been used.			
Gas-gas-interactions				
Ar, He, N_2 [30]	$U(r_{ij}) = 4\varepsilon \left[\left(\frac{\sigma}{r_{ij}} \right)^{12} - \left(\frac{\sigma}{r_{ij}} \right)^6 \right]$ (Lennard-Jones-Potential) where ε is the depth of the potential well, σ is the distance at which the interatomic potential between two particles is zero and r_{ij} is the interatomic distance between the atoms i & j .			
	ε_{ii} [eV]	σ_{ii} [Å]		
$Ar - Ar$ [38]	0.01032	3.4		
$He - He$ [38]	0.00094	2.64		
$N_2 - N_2$ [39]	0.00313	3.32		
Gas-wall-interactions (for FH-mixing rule with parameters from gas-gas-interactions)				
All gas/wall materials[40]	$\sigma_{ij} = \frac{\sigma_{ii} + \sigma_{jj}}{2}$; $\varepsilon_{ij} = \frac{2\varepsilon_{ii} \cdot \varepsilon_{jj}}{\varepsilon_{ii} + \varepsilon_{jj}}$ Fender-Halsey-Mixing-Rule			
Ion pair	ε_{ii} [eV]	σ_{ii} [Å]		
$Si - Si$ [41]	0.00160	0.677		
$Ca - Ca$ [41]	0.01179	1.764		
$O - O$ [41]	0.00875	2.708		

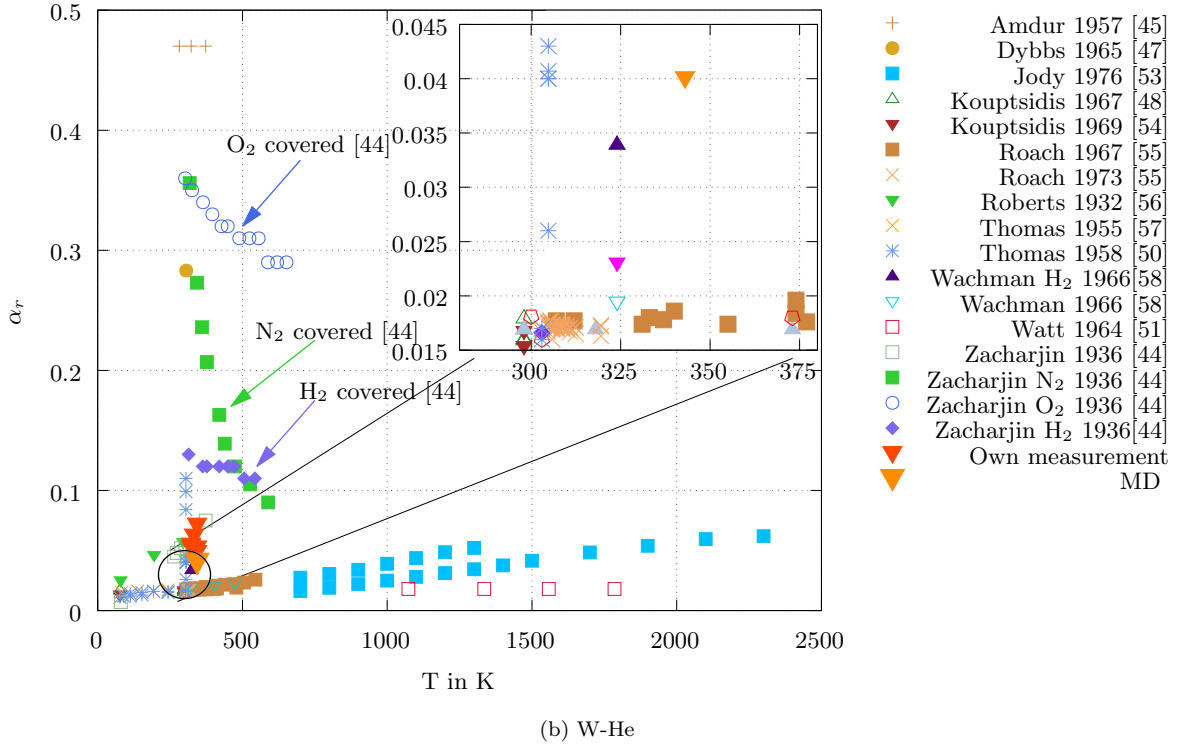
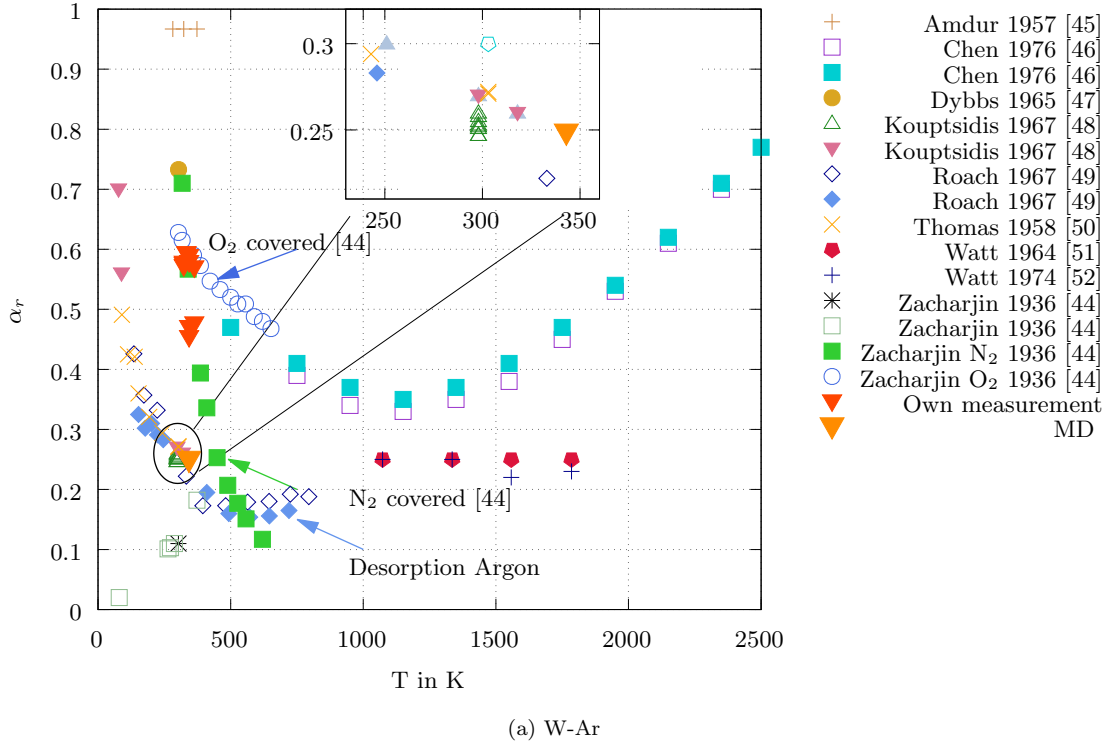


Figure 5: Overview of literature results of α_r over temperature for $W - Ar$ and $W - He$ in comparison with simulation (orange triangles) and experimental results (red triangles, W showed influences of coverage of unknown nature, assumed chemical adsorption): N_2 coverage and desorption examined by Zacharjin [44]

type of thermostat used for controlling the temperatures of NVT regions on the TAC values, is insignificant and also initializing gas velocities with random seed numbers for the given temperature is found to have a negligible effect on α_{cer} due to the sufficient time allowed for the equilibration (see Figure 4).

5.3. Experimental Results

In Figure 7, the final experimental results for $CaSiO_3$ D1 (smoothed surface) are shown versus the molar mass of the used gases in comparison with the results for SiO_2 and $CaSiO_3$ obtained from MD as well as from literature (only SiO_2).

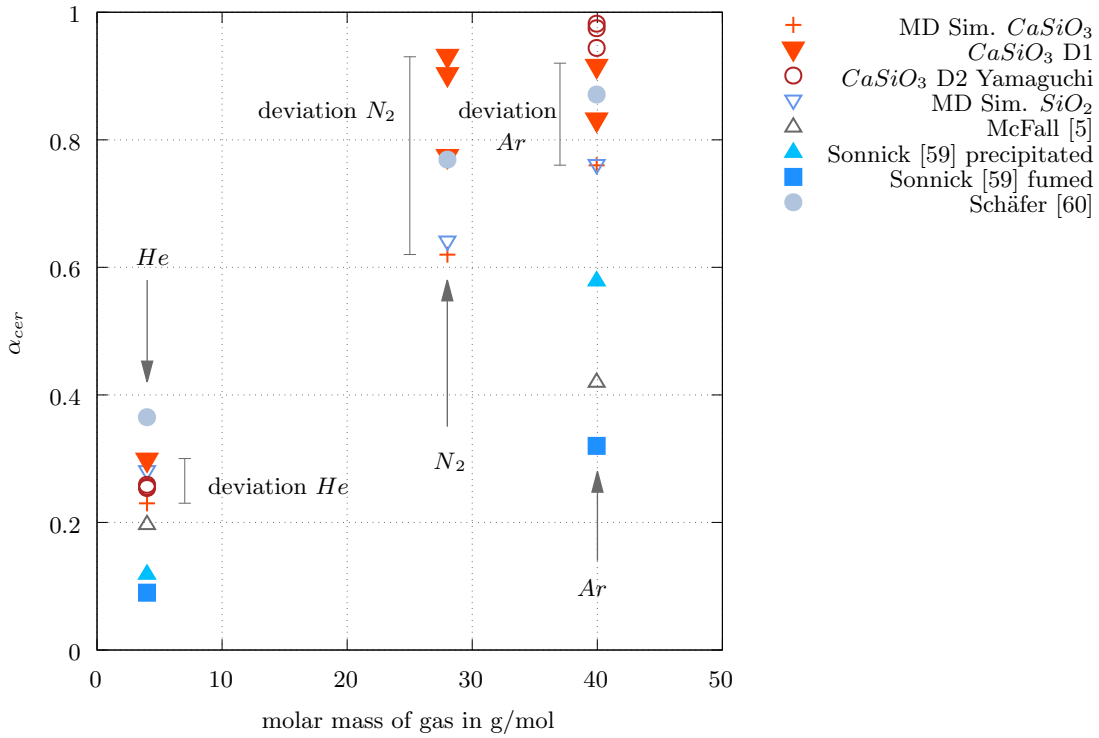


Figure 7: Comparison of experimental (only $CaSiO_3$ D1, D2) and MD results (SiO_2 and $CaSiO_3$) as well as existing literature (only SiO_2) with Ar , N_2 and He over molar mass of used gases; deviations between MD and exp. different for the gases; temperature ca. 345 K for MD and exp., around 300 K for literature, standard uncertainty for own measurements with He $\pm 28\%$ and with Ar/N_2 $\pm 5\%$ (rev 2 pt 3)

Several observations can be found from Figure 7:

- It appears that α_{cer} increases as the molar mass of the used gas increases. For He the lowest values of α_{cer} were achieved as well as for Ar the highest and with N_2 in between. This observation is valid for almost every result except for the experimental results where α_{cer} reaches an equal level for N_2 and Ar .

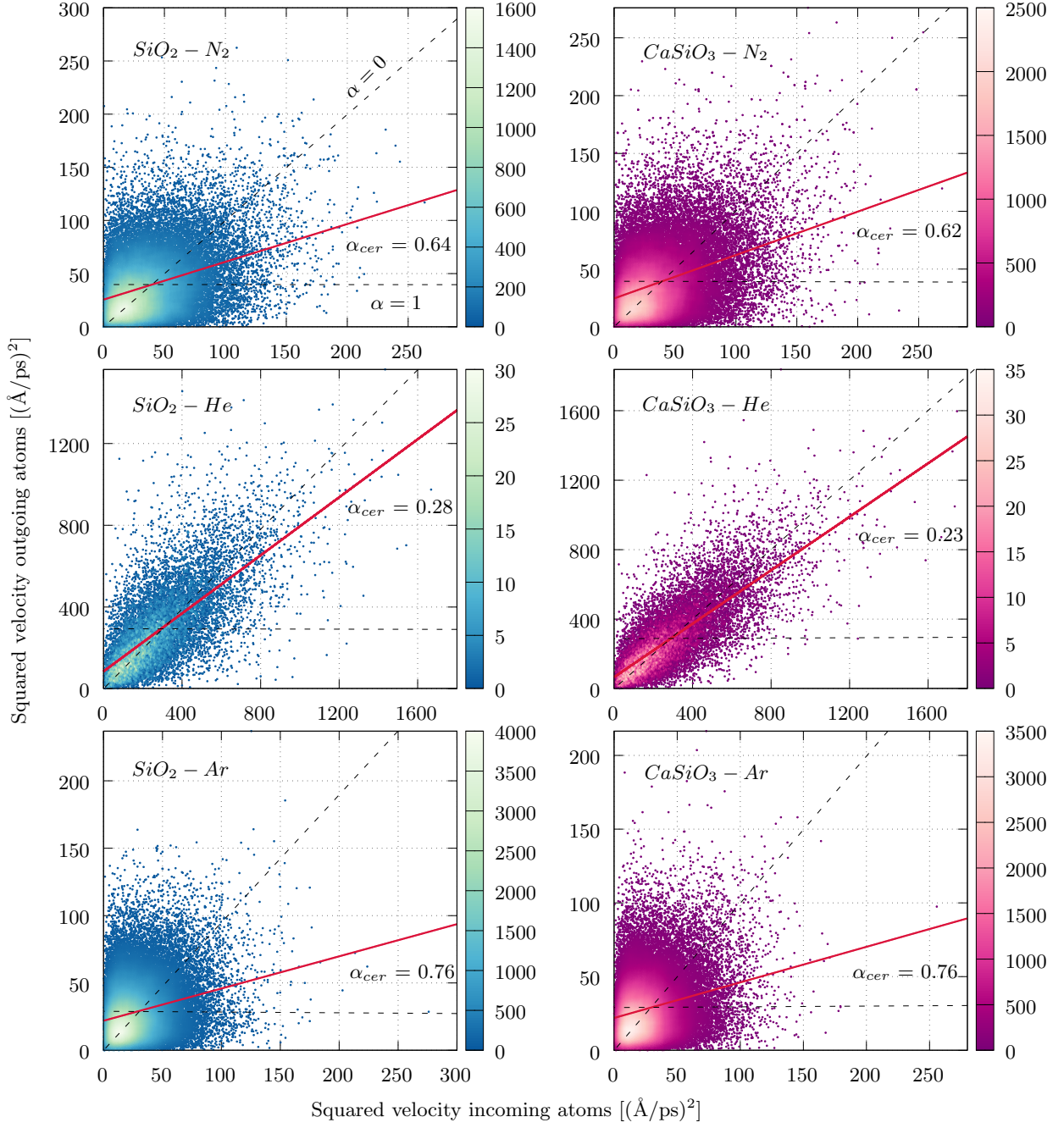


Figure 6: Overview of final results from MD for SiO_2 (blue) and $CaSiO_3$ (pink) with Ar, He and N_2 ; squared velocity of incoming atoms vs. squared velocity of outgoing atoms; diagonal limit (dashed line) $\rightarrow \alpha_{cer} = 0$, horizontal limit (dashed line) $\rightarrow \alpha_{cer} = 1$, red line = result of α_{cer} due to model after Spijker [26] (least squares approximation); palette gives points density

- The results from MD are lower than the experimental results for all gases. However, the deviations between experimental and MD results appear to be different being lowest for *He*, highest for *N₂*, whereas *Ar* lies in between.
- Further promising results were obtained by Yamaguchi and Suzuki in a collaborative work, who used a spherical device for the measurement of α_{cer} (for description of the device see [61]). Their results resemble the experimental data obtained during this work.
- In comparison to literature only those results of Schäfer [60] agree with MD and the present experimental results. The data reported by McFall [5] and Sonnicksen [59] appear to be significantly lower for *He* and even lower for *Ar*.
- An evaluation of the standard uncertainty of the experiments revealed very different values as the standard uncertainty for measurements with *He* reaches up to $\pm 28\%$ whereas with *Ar* and *N₂* a standard uncertainty of $\pm 5\%$ is obtained. (rev 2 pt 3)

Another picture can be drawn from Figure 8. It shows experimental results of *CaSiO₃*-*He* with different porosities (less 5% D1, D2 and 88% A). α_{cer} appears to be higher for higher porosity although no direct correlation could be made concerning the influence of roughness (see Table 1). Further, in this Figure the deviations between the results of MD (0% porosity) and the experiment (*CaSiO₃* D1 and D2 less than 5% porosity) appear to show a very slight influence of porosity, whereas this is further discussed in the following section. Unfortunately, due to the difficulties in measurement and time constraints posed on the current work, further data is unavailable. We note, however, that this raises interesting questions for future research.

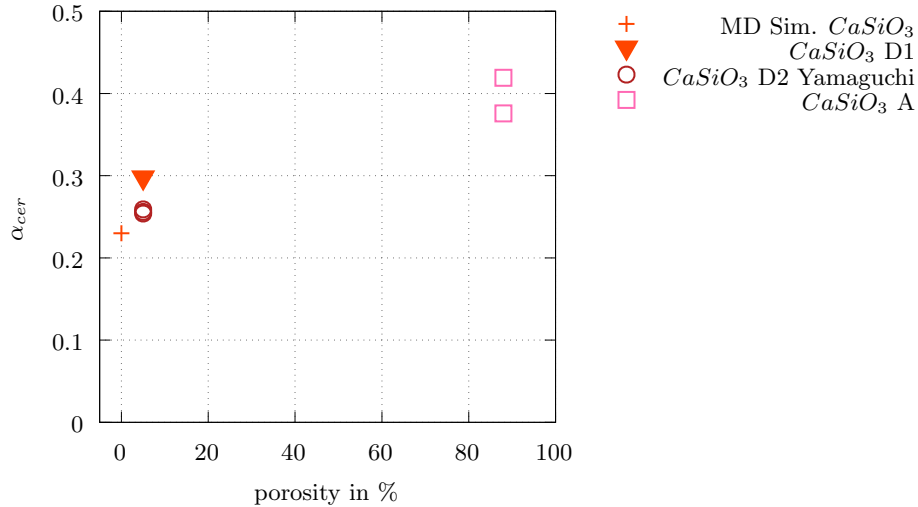


Figure 8: Overview of experimental and simulation results of *CaSiO₃* with *He* over porosity; high porosity only for sample *CaSiO₃* A available; temperature ca. 345 K

5.4. Discussion

In the following a discussion of all obtained results is provided as several issues can be highlighted from Figures 6, 7 and 8:

1. A comparison between the experimental and molecular dynamic results shows a similar increasing trend versus the molar mass, although the values from MD are lower. This increasing trend is a well-known and expected behavior which was highlighted in literature (e.g. see Saxena & Joshi [6]) and also in earlier simulation studies [11, 13]. This point also demonstrates the validity of MD. Furthermore, the results of the MD can be used as a lower limit for α_{cer} on SiO_2 & $CaSiO_3$ since they are determined on free surfaces, i.e. without taking adsorption effects and surface roughness into account. In the course of this ideal limit, based on the experimental results, an influence can be assumed since the deviations between the experimental and molecular-dynamic results are different. To discuss this further, one look back to Figure 5: Zacharjin [44] carried out very interesting measurements by showing the influence of adsorption layers of contaminating gases. The authors were able to show that Ar , in the absence of external contamination, is desorbed significantly faster with increasing temperature (lower α_{W-Ar}) than when a N_2 adsorption layer is present (higher α_{W-Ar}). Accordingly, although N_2 has a lower molar mass than Ar , there is a higher enthalpy of adsorption for N_2 and thus a fundamentally higher thermal accommodation coefficient in general, which is also observed in the literature for other combinations of N_2 (e.g. near room temperature $W - N_2$: $\alpha_{W-N_2} \approx 0.5$ or $Pt - N_2$: $\alpha_{Pt-N_2} \approx 0.8$, see Saxena & Joshi [6]) as well as in everyday laboratory work [62].

A similar behavior can be seen for the experimental results on $CaSiO_3$ D1. Regarding the MD simulation for $CaSiO_3$ D1- Ar a higher value for α_{cer} can be expected due to the higher molar mass of Ar than for $CaSiO_3$ D1- N_2 . Nevertheless, the values for $CaSiO_3$ D1- N_2 are on a similar level as for $CaSiO_3$ D1- Ar representing a significantly greater influence of an N_2 adsorption layer.

2. The experimental results of Yamaguchi and Suzuki ($CaSiO_3$ D2) agree very well with experimental results ($CaSiO_3$ D1). Furthermore, their results continue to exhibit similar deviations in comparison to MD which could be attributed to adsorption. Therefore, it empowers the assumption of an adsorptive influence on the surface and confirms our results.
3. The results of Sonnick et al. [59] with precipitated and fumed silica are not of experimental nature. For the calculation of the thermal accommodation coefficient the model of Kaganer [63] was used exclusively based on the molecular masses of gas and wall molecules. This model neglects any influences like temperature or adsorption or roughness, which can have major contributions to α . Further the experimental validation of Kaganers model fails as it cannot predict well-measured thermal accommodation coefficients, e.g. $\alpha_{W-Ar,exp} = 0.27$ vs. $\alpha_{W-Ar,Kaganer} = 0.58$ (at 300 K). Therefore, the validity of the results for precipitated and fumed silica are questionable until the experimental proof. (rev 2 pt 1)

4. The data obtained by McFall [5] are significantly lower. By examining the obtained data of McFall [5] one can see that a steady state has not been reached by the end of the measurements as it was also stated in report of McFall [5]. This opens the question of a continuous surface contamination which can have a huge impact on α as with increasing surface contamination the thermal accommodation coefficient increases, too [6]. (rev 2 pt 2)
5. From MD the results of amorphous SiO_2 (blue cross) and $CaSiO_3$ (red cross) reach very similar values for all examined gases (see Figure 7). The reason for this close agreement can be attributed to their similar composition and certain similar short range order structural features such as the SiO_4 tetrahedron, and most importantly to the usage of the same gas-ion interaction potential parameter values for the dominant species Si & O in both the cases. In addition, the gas-wall potential depth, which strongly influences values of α_{cer} , was also comparable for both, the Ca and O ions.
6. In MD, the slightly increasing difference of α_{cer} between SiO_2 and $CaSiO_3$ with decreasing molar mass of the gas, although the mass of the solid increases from SiO_2 to $CaSiO_3$, is attributed to the existence of Ca . As per the hard sphere model (which accounts only for direct specular collisions as observed in He), a large mismatch in molar mass between the gas (Ar, N_2, He) molecules and the solid (Ca) leads to inefficient energy transfer between them [13]. Particularly for the case of $CaSiO_3-He$, the heavier Ca (relative to the He atom \rightarrow mass of He / mass of $Ca = 0.1$) could be a potential reason for the reduction of α_{cer} as compared to SiO_2 .
7. The last discussion point is for the measurement of $CaSiO_3$ A-He. The porosity of $CaSiO_3$ A is 88%. Although the porosity and the surface roughness have no recognizable relationship, a higher α_{cer} is observed, which would be expected with a higher surface roughness (compare Table 1). One reason for this behavior could be due to the open porosity, where the gas particles also fly into the porous sample and collide very often with the solid structure resulting in an individual α close to 1. After a (longer) phase within the sample they return to the surface and fly into the free space of the gas gap. Since not every particle “dips” into the open-pored structure, it can be assumed that this effect only occurs in part. To investigate this effect further, the aim was to progress with the measurement of $CaSiO_3$ A-Ar. Unfortunately, however, it was not possible to determine the thermal accommodation coefficient because, as can be seen in Figure 9, there was a different trend of the measuring points (red crosses) over the Knudsen number in comparison to the model curve of λ_{Gas} (blue line). A calculation of α_{cer} in this situation is not possible. λ_{eff} for $CaSiO_3$ B (dotted line), which is very similar to $CaSiO_3$ A and was measured separately, increases in the range of measurability influencing the trend of λ_{Gas} significantly, whereby the experimental values cannot be fitted to Springer’s model.

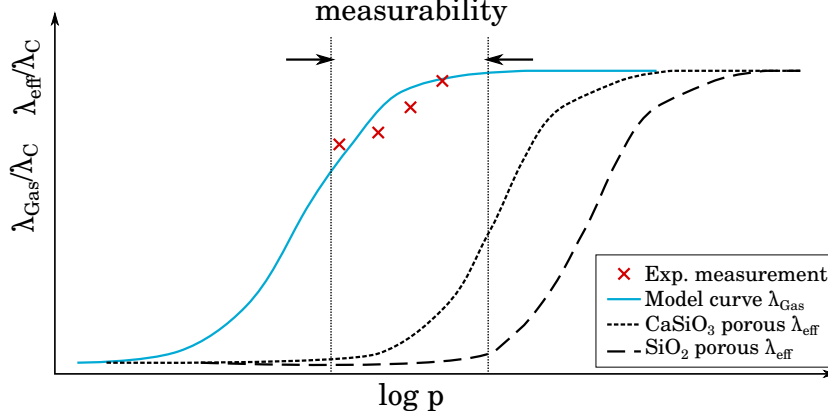


Figure 9: Scheme measurability of $CaSiO_3$ A with Ar, qualitative trends, thermal conductivity of gas and overall (effective) respectively over logarithmic pressure; blue line: model curve of gas thermal conductivity after Springer [17], red crosses: measurement points, dotted line: effective thermal conductivity of highly porous $CaSiO_3$ B, dashed line: effective thermal conductivity of highly porous SiO_2

6. Conclusions

A collaborative study between experiments and atomistic simulations on the determination of thermal accommodation coefficients on amorphous $CaSiO_3$ and SiO_2 with different gases is presented. The thermal accommodation coefficient α , which is amongst other applications a part of the effective thermal conductivity of highly porous insulation materials, is usually set to unity for gases like Ar and N_2 and 0.3 for He over a wider temperature range, but it remained experimentally unverified leaving the reliability of existing models of the effective thermal conductivity in question. This open question was addressed using experimental measurements as well as molecular dynamics simulations and the results are in good agreement (with explainable deviations) with this widely used assumption. It also confirms the validity of using this assumption in models of the effective thermal conductivity. However, these results are only valid near room temperatures and molecular dynamics results showed no significant effect on α (only 1% difference) by varying temperatures ± 20 K around the room temperature, thus demanding no further investigation of this influence from the experimental side in such short temperature range. But from literature, significant influences on α at elevated and cryogenic temperatures are expected and could be an open topic for future research, especially using atomistic simulations. Further, though the influence of surface roughness, contamination and open porosities could not be examined robustly, due to insufficient measurement data to support clear scientific claims, yet some interesting observations are made which provide options to future research.

7. Acknowledgements

Special thanks goes to Prof. Hiroki Yamaguchi and Mr. Yuta Suzuki from the University of Nagoya/Japan as they provided comparative measurements of α on $CaSiO_3$. Their work greatly supports the validity of the results of this work.

Further, great thanks goes to Dr. Claudia Voigt, who successfully prepared the sample $CaSiO_3$ D1, which represents a very important part of this work.

Computing time was provided by the high performance computing cluster (HPC) at TU Freiberg.

Funding: This work was supported by the German Research Foundation (DFG, GR1060/14) and a scholarship by the Saxon Ministry of Science and Art.

References

References

- [1] K. Swimm, G. Reichenauer, S. Vidi, H. Ebert, Gas pressure dependence of the heat transport in porous solids with pores smaller than 10 μm , International Journal of Thermophysics 30 (2009) 1329–1342. doi:10.1007/s10765-009-0617-z.
- [2] K. Swimm, Experimentelle und theoretische untersuchungen zur gasdruckabhängigen wärmeleitfähigkeit von porösen materialien, Ph.D. thesis, Julius-Maximilians-Universität Würzburg (2016).
- [3] J.-J. Zhao, Y.-Y. Duan, X.-D. Wang, B.-X. Wang, Effects of solid-gas coupling and pore and particle microstructures on the effective gaseous thermal conductivity in aerogels, Journal of Nanoparticle Research 14 (8).
- [4] E. Litovsky, M. Shapiro, A. Shavit, Gas pressure and temperature dependences of thermal conductivity of porous ceramic materials: Part 2, refractories and ceramics with porosity exceeding 30 %, Journal of the American Ceramic Society 79 (1996) 1366–1376.
- [5] A. McFall, The thermal accommodation coefficient of helium and argon on an amorphous SiO_2 surface, Master (1980).
- [6] S. Saxena, R. Joshi, Thermal Accommodation and Adsorption Coefficients of Gases, Hemisphere Publishing Corporation, 1989.
- [7] ZichunYang, G. Su, B. Chen, Molecule dynamics study on heat transfer at gas-nanoparticle interface, CMC-COMPUTERS MATERIALS & CONTINUA 51 (1) (2016) 43–62.

- [8] T. Feng, A. Rai, D. Hun, S. S. Shrestha, Molecular dynamics simulations of energy accommodation between gases and polymers for ultra-low thermal conductivity insulation, *International Journal of Heat and Mass Transfer* 164 (2021) 120459. doi:<https://doi.org/10.1016/j.ijheatmasstransfer.2020.120459>.
URL <https://www.sciencedirect.com/science/article/pii/S0017931020333950>
- [9] T. Sipkens, K. Daun, Effect of surface interatomic potential on thermal accommodation coefficients derived from molecular dynamics, *The Journal of Physical Chemistry C* 122 (35) (2018) 20431–20443.
- [10] J. Sun, Z.-X. Li, Three-dimensional molecular dynamic study on accommodation coefficients in rough nanochannels, *Heat transfer engineering* 32 (7-8) (2011) 658–666.
- [11] S. Mohammad Nejad, S. Nedea, A. Frijns, D. Smeulders, The influence of gas–wall and gas–gas interactions on the accommodation coefficients for rarefied gases: A molecular dynamics study, *Micromachines* 11 (3) (2020) 319.
- [12] F. O. Goodman, Thermal accommodation coefficients, *The Journal of Physical Chemistry* 84 (12) (1980) 1431–1445.
- [13] Z. Liang, P. Keblinski, Parametric studies of the thermal and momentum accommodation of monoatomic and diatomic gases on solid surfaces, *International Journal of Heat and Mass Transfer* 78 (2014) 161–169.
- [14] K. Raed, U. Gross, Review on gas thermal conductivity in porous materials and knudsen effect, in: *Proceedings of the 29th international thermal conductivity conference*, Birmingham, Alabama, USA, 2007.
- [15] En 12667 - bestimmung des wärmedurchlasswiderstandes nach dem verfahren mit dem plattengerät und dem wärmestrommessplattengerät, Tech. rep., Europäische Norm (2001).
- [16] D. Bayer, K. Raed, U. Gross, R. Wulf, A new facility for the experimental investigation on nano heat transfer between gas molecules and ceramic surfaces, in: *32nd Int. Thermal Conductivity Conference (ITCC) and 20th Int. Thermal Expansion Symposium (ITES)*, Purdue University, West Lafayette, USA, 2014.
- [17] G. Springer, Heat transfer in rarefied gases, *Advances in Heat Transfer* 7 (1971) 163–218.
- [18] L. Lees, C. Liu, Kinetic theory description of plane, compressible couette flow, Research report, GUGGENHEIM AERONAUTICAL LABORATORY CALIFORNIA INSTITUTE OF TECHNOLOGY (1960).
- [19] F. Sherman, *Rarefied Gas Dynamics*, Vol. 2, Academic Press, 1963.
- [20] Function file: leasqr (x, y, pin, f), <https://octave.sourceforge.io/optim/function/leasqr.html>, accessed: 2021-06-18 (2021).

- [21] R. N. Mead, G. Mountjoy, a molecular dynamics study of the atomic structure of $(\text{cao})_x (\text{sio}_2)_{1-x}$ glasses, *The Journal of Physical Chemistry B* 110 (29) (2006) 14273–14278.
- [22] S. Munetoh, T. Motooka, K. Moriguchi, A. Shintani, Interatomic potential for si–o systems using tersoff parameterization, *Computational Materials Science* 39 (2) (2007) 334–339.
- [23] S. Nosé, A unified formulation of the constant temperature molecular dynamics methods, *The Journal of chemical physics* 81 (1) (1984) 511–519.
- [24] W. G. Hoover, Canonical dynamics: Equilibrium phase-space distributions, *Physical review A* 31 (3) (1985) 1695.
- [25] E. Braun, J. Gilmer, H. B. Mayes, D. L. Mobley, J. I. Monroe, S. Prasad, D. M. Zuckerman, Best practices for foundations in molecular simulations [article v1. 0], *Living journal of computational molecular science* 1 (1).
- [26] P. Spijker, A. J. Markvoort, S. V. Nedeia, P. A. Hilbers, Computation of accommodation coefficients and the use of velocity correlation profiles in molecular dynamics simulations, *Physical Review E* 81 (1) (2010) 011203.
- [27] S. Plimpton, Fast parallel algorithms for short-range molecular dynamics, *Journal of computational physics* 117 (1) (1995) 1–19.
- [28] A. Stukowski, Visualization and analysis of atomistic simulation data with ovito—the open visualization tool, *Modelling and Simulation in Materials Science and Engineering* 18 (1) (2009) 015012.
- [29] A. Pedone, G. Malavasi, M. C. Menziani, A. N. Cormack, U. Segre, A new self-consistent empirical interatomic potential model for oxides, silicates, and silica-based glasses, *The Journal of Physical Chemistry B* 110 (24) (2006) 11780–11795.
- [30] J. E. Jones, On the determination of molecular fields.—ii. from the equation of state of a gas, *Proceedings of the Royal Society of London. Series A, Containing Papers of a Mathematical and Physical Character* 106 (738) (1924) 463–477.
- [31] V. Bakaev, W. Steele, T. Bakaeva, C. G. Pantano, Adsorption of co₂ and ar on glass surfaces. computer simulation and experimental study, *The Journal of chemical physics* 111 (21) (1999) 9813–9821.
- [32] O. Talu, A. L. Myers, Reference potentials for adsorption of helium, argon, methane, and krypton in high-silica zeolites, *Colloids and Surfaces A: Physicochemical and Engineering Aspects* 187 (2001) 83–93.
- [33] M. Ozhgibesov, T. Leu, C. Cheng, A. Utkin, Studies on argon collisions with smooth and rough tungsten surfaces, *Journal of Molecular Graphics and Modelling* 45 (2013) 45–49.

- [34] N. Juslin, B. Wirth, Interatomic potentials for simulation of the bubble formation in w, *Journal of Nuclear Materials* 432 (1-3) (2013) 61–66.
- [35] J. Tersoff, Modeling solid-state chemistry: Interatomic potentials for multicomponent systems, *Physical review B* 39 (8) (1989) 5566.
- [36] M. S. Daw, M. I. Baskes, Embedded-atom method: Derivation and application to impurities, surfaces, and other defects in metals, *Physical Review B* 29 (12) (1984) 6443.
- [37] P. A. Olsson, Semi-empirical atomistic study of point defect properties in bcc transition metals, *Computational materials science* 47 (1) (2009) 135–145.
- [38] J. O. Hirschfelder, C. F. Curtiss, R. B. Bird, M. G. Mayer, *Molecular theory of gases and liquids*, Vol. 165, Wiley New York, 1964.
- [39] H. Zambrano, J. H. Walther, R. Jaffe, Molecular dynamics simulations of water on a hydrophilic silica surface at high air pressures, *Journal of Molecular Liquids* 198 (2014) 107–113.
- [40] B. E. F. Fender, G. D. Halsey, Second virial coefficients of argon, krypton, and argon-krypton mixtures at low temperatures, *The Journal of Chemical Physics* 36 (7) (1962) 1881–1888. [arXiv:https://doi.org/10.1063/1.1701284](https://doi.org/10.1063/1.1701284), doi:10.1063/1.1701284.
URL <https://doi.org/10.1063/1.1701284>
- [41] K. Watanabe, N. Austin, M. Stapleton, Investigation of the air separation properties of zeolites types a, x and y by monte carlo simulations, *Molecular Simulation* 15 (4) (1995) 197–221.
- [42] Powder tech note 27, accessed: 2021-06-23 (2021).
URL www.quantachrome.com
- [43] A. Steinbeck, Methode zur messung von atomarem sauerstoff mittels katalytischem prinzip, Ph.D. thesis (2016).
- [44] G. Zacharjin, G. Spivak, Energy exchange between helium, neon and argon atoms and a metallic surface, *Physikalische Zeitschrift der Sowjetunion* 10 (1936) 495–509.
- [45] I. Amdur, L. Guildner, Thermal accommodation coefficients on gas-covered tungsten, nickel and platinum, *Journal of the American Chemical Society* 79 (1957) 311–315.
- [46] S. Chen, S. Saxena, Thermal accommodation coefficients for the gas-covered tungsten-argon system at high temperatures (600-2500 K), *High Temperature Science* 8 (1) (1976) 1–9.
- [47] A. Dybbs, G. S. Springer, Heat conduction experiments in rarefied gases between concentric cylinders, *The Physics of Fluids* 8 (11) (1965) 1946–1950.

- [48] J. Kouptsidis, D. Menzel, Thermal accommodation of the rare gases on clean metal surfaces, in: H. Saltsburg, J. J. Smith, M. Rogers (Eds.), *Fundamentals of Gas Surface Interactions*, Academic Press, 1967, pp. 493–505.
- [49] D. Roach, L. Thomas, Determination of the thermal accommodation coefficients of gases on clean surfaces at temperatures above 300°K by the temperature jump method, in: *Rarefied Gas Dynamics Fifth Symposium*, Vol. 1, Academic Press, 1967.
- [50] L. Thomas, Studies of the thermal accommodation coefficients of gases on metal surfaces and their relation to the absorbed condition of the surfaces, *Ad* 204 684 (1958) 44.
- [51] W. Watt, R. Moreton, The thermal accommodation of helium and argon on tungsten and platinum at elevated temperatures, Royal Aircraft Establishment Rept. RAE-TN-CPM-8-X65-10984 (1964) 21.
- [52] W. Watt, R. Moreton, L. Carpenter, The thermal accommodation of helium and argon on a tungsten wire, deduced from the heat lost by the wire, *Surface Science* 45 (1974) 238–248.
- [53] B. Jody, S. Saxena, Heat transfer at the solid-gas interface: Thermal accommodation coefficients of helium on gas covered tungsten, *Proceedings of the Fifth All-Union Heat and Mass Transfer Conference in Minsk, USSR*.
- [54] J. Kouptsidis, D. Menzel, Thermal accommodation of the helium isotopes on clean tungsten surfaces, *Zeitschrift für Naturforschung A* 24 (3) (1969) 479–480.
- [55] D. V. Roach, L. B. Thomas, Comparative study of accommodation coefficients of helium and neon on clean tungsten under transition, temperature jump and free molecule conditions, *The Journal of Chemical Physics* 59 (1973) 3395–3402.
- [56] J. Roberts, The exchange of energy between gas atoms and solid surfaces. ii. the temperature variation of the accommodation coefficient of helium, *Proceedings of the Royal Society of London. Series A, Containing Papers of a Mathematical and Physical Character* 135 (826) (1932) 192–205.
- [57] L. Thomas, E. Schofield, Thermal accommodation coefficient of helium on a bare tungsten surface, *The Journal of Chemical Physics* 23 (5) (1955) 861–866.
- [58] H. Y. Wachman, Thermal accommodation coefficients of helium on tungsten and hydrogen on hydrogen-covered tungsten at 325 K, *The Journal of Chemical Physics* 45 (1966) 1532–1538.
- [59] S. Sonnick, M. Meier, J. Ross-Jones, L. Erlbeck, I. Medina, H. Nirschl, M. Rädle, Correlation of pore size distribution with thermal conductivity of precipitated silica and experimental determination of the coupling effect, *Applied Thermal Engineering* 150 (2019) 1037–1045. doi:<https://doi.org/10.1016/j.applthermaleng.2019.01.074>.
URL <https://www.sciencedirect.com/science/article/pii/S1359431118374842>

- [60] K. Schäfer, K. Riggert, Ein verfahren zur ermittlung partieller thermischer akkommodationskoeffizienten, *Journal of Colloid Science* 9 (1954) 128–134.
- [61] H. Yamaguchi, T. Imai, T. Iwai, A. Kondo, Y. Matsuda, Measurement of thermal accommodation coefficients using a simplified system in a concentric sphere shell configuration, *Journal of Vacuum Science and Technology A: Vacuum, Surfaces, and Films* 32 (6) (2014) 061602.
- [62] V. Jakobi, experiences from laboratory work, personal comment (2021).
- [63] M. Kaganer, Thermal insulation in cryogenic engineering, Israel Program for Scientific Translations (Jerusalem), 1969.